PCCP

ROYAL SOCIETY OF CHEMISTRY

PAPER

Cite this: *Phys. Chem. Chem. Phys.*, 2023, **25**, 14257

Advanced optical terahertz fingerprint sensor based on coherent perfect absorption†

You Ran Wu, [a] Rui Yang Dong,[b] Jia Hao Zou[a] and Hai Feng Zhang *[a]

Received 7th February 2023,
Accepted 7th May 2023

DOI: 10.1039/d3cp00592e

rsc.li/pccp

An advanced optical terahertz (THz) fingerprint sensor based on coherent perfect absorption (CPA) is proposed. Based on a one-dimensional layered photonic structure, the sensor contains a cavity that is developed for THz fingerprint measurement. Utilizing the magneto-optical effect of magnetized InSb, CPA is excited in the structure of the sensor. Taking α-lactose as exemplar material, this numerical simulation is integrated with a Drude–Lorentz model. The transfer matrix method (TMM) is used to calculate the sensitivity (*S*), linear range (LR), quality (*Q*), the figure of merit (FOM*), and detection limit (DL) theoretically. Employing the amplitude modulation detection method, the qualitative and quantitative analysis of the α-lactose thickness of 0–0.5 μm could be realized. Because of the fragility of CPA, the *S* is 0.78255 μm^{-1}, the value of average *Q* is up to 8019.2, the value of average FOM* is 13 234.4 $(THz\ \mu m)^{-1}$, and the lower DL is 4.21×10^{-6}. Moreover, the evolutions of ensemble-averaged absorption in the vicinity of the absorption peaks for different types of disorder effects are considered, which will be considered in the fabrication of sensors.

1. Introduction

Coherent perfect absorption (CPA),[1] a new optical scheme that generates high absorption in devices with negligible inherent losses,[2,3] has aroused widespread concern owing to its potential for the dynamic tunability of absorption and all-optical logical processes.[4,5] Associated with time-reversal symmetry, the time-reversal process of laser emission is the theoretical basis of CPA.[1,6] By interfering with two incident electromagnetic (EM) waves, CPA is realized in the structure of an optical sensor, which contains a multipass interferometer such as a Fabry–Perot resonator only when both beams have the right relative phase and amplitude. As a result, it is sensitive to the amplitude of EM waves. Additionally, it can also be utilized as an absorption interferometer, potentially useful as a modulator and detector. Conditions for implementing CPA have been derived theoretically and verified experimentally.[6] To describe and predict the state of CPA more effectively, the scattering matrix is utilized. It follows that CPA frequently happens on narrow bands since the eigenvalue of the scattering matrix must be zero for CPA to occur.[7] As a result, selecting the suitable system setup and configurations is necessary for achieving CPA and CPA is particularly sensitive to tiny variations in the parameters of the sample to be detected. Furthermore, while the relative amplitude of two incident EM waves altered, the absorption should theoretically be adjusted from 50% to 100%. Meanwhile, under certain configurations, even little changes in the sample might result in a significant decrease in absorption. Hence, adjusting the relative amplitude to maintain the absorption at a specific value for sensing is considered. There are cases of absorbers made using narrow-band THz absorption peaks,[8] which will have applications in sensing.[9–11] Similarly, CPA has the potential to be employed as optical terahertz (THz) fingerprint sensors, while few investigations have been conducted so far. To implement the functionality of THz fingerprint detection using THz spectroscopy in a conventional absorption scheme, fundamentally, one has to be concentrated on two characteristics.[12] The first is the characteristic frequency, which is the spectral qualities of a particular sample and appears as resonances in the absorption spectrum; the second is the variation in the absorption peak at the characteristic frequency, which implies the changes in thickness in the sample. In 2018, A method for high-precision position sensing based on the mechanism of CPA in a layered structure was proposed by Dey *et al.*[13] In 2019, Li *et al.* established a graphene sensor with complete light confinement within a monolayer of graphene that doesn't necessitate nanofabrication.[14] A simple construction using a single sheet of graphene was used to obtain high-sensitivity CPA, with a sensitivity of over 440 000 nm RIU^{-1} at the wavelength of 1 μm. In 2022, Zhang *et al.* proposed a theoretical refractive index sensing model based on the CPA mechanism that utilizes phase modulation for absorption compensation.[15] With the largest figure of merit (FOM*) value of 1874.9 RIU^{-1}, their presented sensing method is a promising high-sensitivity detection scheme.

[a] *College of Electronic and Optical Engineering & College of Flexible Electronics (Future Technology), Nanjing University of Posts and Telecommunications, Nanjing, 210023, China. E-mail: hanlor@163.com*

[b] *Bell Honors School & Intensive Courses in Science and Engineering, Nanjing University of Posts and Telecommunications, Nanjing, 210023, China*

† Electronic supplementary information (ESI) available. See DOI: **https://doi.org/10.1039/d3cp00592e**

Specific identification of molecules is necessary for many biochemical processes, and therefore the need for sensitive biomolecular sensing methods has dramatically increased.[16] Particularly, many biochemical molecules experience intramolecular and intermolecular vibrations in the THz region, which gives this region the advantage of detecting molecular absorption peaks. Because the absorption peaks of molecules are as unique as human fingerprints, we also call this kind of detection THz fingerprint detection. Herein, α-lactose is applied as a test substance, because it is nonpoisonous, relatively inert, and has narrow linewidth in its low-THz range resonances. Due to its abundance in both human and domestic animal milk, α-lactose is a very significant sugar. α-lactose is a crucial asset as a fundamental ingredient and the primary substrate in fermentative processes that result in fermented milk products like yogurt and kefir. α-Lactose can be also used as analytical reagents, chromatographic analysis reagents, and used in the preparation of biological media. In 2020, Zhu *et al.* suggested a technique based on THz wave angular scanning on a dielectric metagrating.[17] By adjusting the polarization and incidence angle in various trace-amount analytes owing to guided-mode resonance, the local electric field could well be strengthened, significantly enhancing the broadband signal of the molecular fingerprint. In 2021, Ding *et al.* suggested an all-dielectric lithography-free sensor to boost THz absorption using an evanescent wave, which can provide a coupled mode with high detecting capability.[18]

Considering the adaptability of the CPA, this paper proposed an advanced optical sensor utilizing amplitude modulation for THz fingerprint detection. Due to the fragility of CPA, the sensor performs excellently with high sensitivity (S), high quality (Q), high FOM*, and lower detection limit (DL). Disorder effects are considered to demonstrate a slight effect on measurements due to the manufacturing process and external environment.

2. Design and discussion

2.1. Theoretical model

Fig. 1 depicts the schematic diagram of an advanced THz fingerprint sensor that has increased sensitivity for detecting THz fingerprints. It is simple and reliable to capture a sample that is only a few tens of nanometers thick. The structure of the sensor is illuminated by two counter-propagating EM waves, approaching the surface with an incident angle θ. To realize CPA, the two EM waves have the same phase and amplitude. The structure comprises two parallel Bragg reflectors which are composed of four silicon (Si) stacks separated by air respectively and thin layers of magnetized indium antimonide (InSb) dispersed on both sides and one center defect cavity. As the carrier for samples, one thin Teflon with a thickness of 50 μm is positioned in the center of the cavity. The external magnetic field B is parallel to the y-axis. Herein, magnetized InSb layers are introduced for their magneto-optic effect to modulate the electromagnetic waves to achieve coherent perfect absorption. As a narrow gap semiconductor, InSb has excellent optical properties in this band and manipulates light more significantly in the THz band. Affected by Lorentz's force, only the EM waves with TM polarization, which propagate in magnetized InSb layers, can be magnetically controlled. Therefore, this article will concentrate on investigating the magnetic-controlled performance under TM polarization. The thickness of three common dielectrics, denoted by d_{Si}, d_{air}, and d_{Teflon}, are d_{Si} = 100 μm, d_{air} = 233 μm, and d_{Teflon} = 50 μm. The length of the cavity is selected as d_{cavity} = 268 μm. The thickness of semiconductor InSb is fixed to d_{InSb} = 0.8 μm. The refractive indexes (RIs) of common dielectrics are set as n_{Si} = 3.44,[19] n_{air} = 1, and n_{Teflon} = 1.46,[12] respectively. Besides, the transmission characteristic is analyzed by the transfer matrix method (TMM). When the EM waves incident vertically, the incident angle θ is 0 degrees. The concentration of the free carriers in the InSb layer is given by the empirical formula below.[20,21]

$$N(\mathrm{m}^{-3}) = 5.76 \times 10^{14} T_0^{1.5} \exp[-0.26/(2 \times 8.625 \times 10^{-5} \times T_0)] \quad (1)$$

Additionally, N has a significant impact on the dielectric characteristics of InSb, which are highly dependent on the temperature T_0 (T_0 takes 303 K). For InSb, the effective carrier mass m^* is related to the mass of electron m_e: $m^* = 0.0015 m_e$.

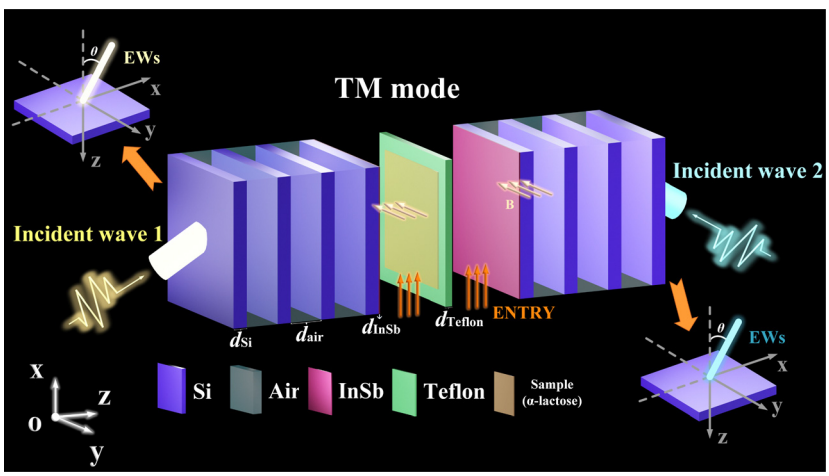

Fig. 1 The schematic diagram of the THz fingerprint sensor.

The plasma frequency ω_{p1} is determined by the free carrier density and the effective carrier mass m^* as follows:[22]

$$\omega_{p1} = \sqrt{\frac{e^2 N}{\varepsilon_0 m^*}} \tag{2}$$

where ε_0 and e indicate the permittivity in a vacuum and the electron charge, respectively.

Under the external magnetic field along the y-direction, magnetized InSb is an anisotropic medium, whose effective permittivity is a tensor and has the following form:[20]

$$\varepsilon_{InSb} = \begin{pmatrix} \varepsilon_x & 0 & \varepsilon_{xz} \\ 0 & \varepsilon_y & 0 \\ -\varepsilon_{xz} & 0 & \varepsilon_x \end{pmatrix} \tag{3}$$

where

$$\varepsilon_x = \varepsilon_{\infty 1} - \varepsilon_{\infty 1}\frac{\omega_{p1}{}^2(\omega + j\nu_c)}{\omega\left[(\omega + j\nu_c)^2 - \omega_c{}^2\right]} \tag{4}$$

$$\varepsilon_y = \varepsilon_{\infty 1} - \varepsilon_{\infty 1}\frac{\omega_p{}^2}{\omega(\omega + j\nu_c)} \tag{5}$$

$$\varepsilon_{xz} = \varepsilon_{\infty 1}\frac{j\omega_{p1}{}^2\omega_c}{\omega\left[(\omega + j\nu_c)^2 - \omega_c{}^2\right]} \tag{6}$$

Herein, ω denotes the angle frequency, ν_c is the carrier collision frequency, and $\varepsilon_{\infty 1}$ is the high-frequency limit permittivity, taken as 15.68. According to the formula $\omega_c = eB/m^*$, a high gyrotropy near the cyclotron frequency ω_c corresponds proportional to the external magnetic field, and the initial value of B is 1.23 T.

Under the TM polarization, the effective reflective index of InSb is attained:[23]

$$n_{TM} = \sqrt{\frac{\varepsilon_x{}^2 - \varepsilon_{xz}{}^2}{\varepsilon_x{}^2}} \tag{7}$$

Based on the boundary conditions, the transmission matrix can be deduced:[24]

$$M_{InSb} = \begin{pmatrix} \cos(k_z d) + \sin(k_z d)\cdot\dfrac{k_x\varepsilon_{xz}}{k_z\varepsilon_x} & -\dfrac{j}{\eta}\left[1 + \left(\dfrac{k_x\varepsilon_{xz}}{k_z\varepsilon_x}\right)^2\right]\cdot\sin(k_z d) \\ -j\eta\sin(k_z d) & \cos(k_z d) - \sin(k_z d)\cdot\dfrac{k_x\varepsilon_{xz}}{k_z\varepsilon_x} \end{pmatrix} \tag{8}$$

where $k_x = \omega\, n_{TM}\sin\theta/c$ and $k_z = \omega\, n_{TM}\cos\theta/c$ denote the inverse elements of the wave vectors at x- and z-axis, $\eta = (\varepsilon_0/\mu_0)^{1/2}\, n_{TM}/\cos\theta$ is the optical admittance.

When the α-lactose layer is deposited on the Teflon film in the cavity, the coherent absorption will be significantly influenced by its intrinsic loss. To describe this material resonance, one can obtain the permittivity of α-lactose using the dielectric function such as the Drude–Lorentz model;[25,26]

$$\varepsilon_r = \varepsilon_{\infty 2} + \sum_{p=1}^{\infty}\frac{\Delta\varepsilon_p\omega_{p2}{}^2}{\omega_{p2}{}^2 - \omega^2 - j\gamma_p\omega} \tag{9}$$

where $\varepsilon_{\infty 2}$ stands for the background permittivity of α-lactose off this resonance. $\Delta\varepsilon_p$ is the strength factor of this resonance, ω_{p2} is the angular frequency of absorption oscillation, and γ_p is the resonance bandwidth. For simplification, only the first-order absorption resonance of α-lactose at 0.53 THz is taken into account and these four parameters are fixed to: 3.145, 0.052, $2\pi \times 0.53 \times 10^{12}$ rad s^{-1} and $2\pi \times 25.3 \times 10^9$ rad s^{-1}, respectively.[27]

As for conventional dielectric layers, the transfer matrix is:[24,28]

$$M_i = \begin{pmatrix} \cos\delta_i & -j\sin\delta_i/\eta_i \\ -j\eta_i\sin\delta_i & \cos\delta_i \end{pmatrix} (i = \text{Si, Teflon, air, α-lactose}) \tag{10}$$

where $\delta_i = -2\pi\, n_i\, d_i\cos\theta_i/\lambda$ and $\eta_i = (\varepsilon_0/\mu_0)^{1/2}\, n_i\cos\theta_i$.

When the EM wave passes through the structure of the sensor, the entire transmission matrix, which connected the input and output EM field can be deduced by analogy. The TMM is utilized to connect various media layers in the following ways:

$$M = \begin{pmatrix} m_{11} & m_{12} \\ m_{21} & m_{22} \end{pmatrix} \tag{11}$$

The reflection coefficient R_c and transmission coefficient T_c are as follows,[29]

$$R_c = |r|^2, \tag{12}$$

$$T_c = |t|^2 \tag{13}$$

where

$$r = \frac{(m_{12}\eta_{N+1} + m_{11})\eta_0 - (m_{22}\eta_{N+1} + m_{21})}{m_{11}\eta_0 + m_{21}m_{12}\eta_0 + \eta_{N+1} + m_{22}\eta_{N+1}}, \tag{14}$$

$$t = \frac{2\eta_0}{m_{11}\eta_0 + m_{21} + m_{22}\eta_{N+1} + m_{12}\eta_0\eta_{N+1}}, \tag{15}$$

And $\eta_0 = \eta_{N+1} = (\varepsilon_0/\mu_0)^{1/2}\, n_0/\cos\theta_0$ in the TM mode. Therefore, the absorption can be presented as:

$$A = 1 - |r|^2 - |t|^2, \tag{16}$$

The construction of the THz fingerprint sensor is symmetrical. Consequently, the numerical values of the transmission and reflection coefficients in the front and back are equal, simplifying with $t_+ = t_- = t$, $r_+ = r_- = r$. Considering the interaction of two counter-propagating EM waves, the forward and backward scattering EM fields (O_+ and O_-) can be obtained from the incident of forward and backward waves (I_+ and I_-), respectively, and can be expressed as:

$$\begin{pmatrix} O_+ \\ O_- \end{pmatrix} = S\begin{pmatrix} I_+ \\ I_- \end{pmatrix} = \begin{pmatrix} t & r \\ r & t \end{pmatrix}\begin{pmatrix} I_+ \\ I_- \end{pmatrix}, \tag{17}$$

The equation can also be given as:[30]

$$O_+ = t|I_+|e^{i\phi_+} + r|I_-|e^{i\phi_-}, \tag{18}$$

$$O_- = r|I_+|e^{i\phi_+} + t|I_-|e^{i\phi_-}, \tag{19}$$

where φ_+, and φ_- are the phases of two incident waves. Accordingly,

the coherent absorptance may be written as follows:

$$A_c = 1 - \frac{|O_+|^2+|O_-|^2}{|I_+|^2+|I_-|^2}, \quad (20)$$

Combining eqn (18)–(20), it is attainable that:

$$A_c = 1 - (|t| - |r|)^2 - 2|t||r| \times \left(1 + \frac{2|I_+||I_-|\cos\Delta\varphi_1 \cos\Delta\varphi_2}{|I_+|^2+|I_-|^2}\right), \quad (21)$$

where $\Delta\varphi_1$ = Arg(t) − Arg(r), where Arg() represents the argument principal value of the plural. And $\Delta\varphi_2 = \varphi_+ - \varphi_-$. To realize CPA, the following conditions should be satisfied: (1) $|I_+| = |I_-|$, (2) $\cos\Delta\varphi_1\cos\Delta\varphi_2 = -1$, (3) $|t| = |r|$. In addition, modulation of the coherent absorption can be achieved by controlling the amplitudes of the incident EM waves.

The proposed sensor mainly considers the detection in TM mode, as the calculation in TE mode can be found in Section S1 of ESI.†

2.2. Analysis and discussion

Based on the previously specified structural arrangement of the sensor, the transmission characteristics are computed using the TMM. As shown in Fig. 2(a), an extremely narrow absorption band occurs at the frequency of 0.474729 THz, and the absorption peak reaches 0.998365, which can be regarded as CPA. Meanwhile, The absorption peak is particularly sharp, having a full-width at half-maximum bandwidth of 3.6 × 10^{-5} THz, eventually leading to a high Q of more than 13 197 and CPA through this device that can go approach 100% at resonance. As demonstrated in Fig. 2(b) and (c), the conditions of CPA are satisfied. At the resonant frequency, both transmittance and reflectance are equal to 0.25, and the $\cos\Delta\varphi_2$ is equal to −1. Given the counter-propagating EM waves, they have the same amplitude and phase. Therefore, All the conditions are satisfied to realize CPA. Meanwhile, Fig. 2(b) indicates that the maximal absorption is 0.5 when an EM wave incident from one side. As demonstrated in the 3-D plot in Fig. 2(d), the absorption may be modulated continuously by altering the relative amplitude of the incident EM waves. It is crucial to note that the spectrum of absorption exhibits a small region of high absorptance when the two incident waves have the same amplitude, with the highest absorption of 0.998365. As the relative amplitude deviates, the absorptance decreases. When the amplitude of one incident wave is half that of the other, the coherent absorption is 0.8996. The absorption is reduced to 0.499807 when one of the incident waves disappears completely.

The magnetic field distribution of the device at various frequencies is shown in Fig. 3. The schematic diagrams are done by the finite element method (FEM) to approximate. Due to the discrepancy between TMM and FEM, the frequency of absorption peaks red-shifts. When the frequency is 0.46243 THz, one can notice that the energy is focused inside the apparatus, reaching H = 1.2 × 10^3 A m^{-1}, which suggests that the EM waves are confined and subsequently absorbed by the device. Furthermore, as plotted in Fig. 3(b), the energy is distributed in the various parts of the structure of the sensor, with the highest H = 12 A m^{-1}.

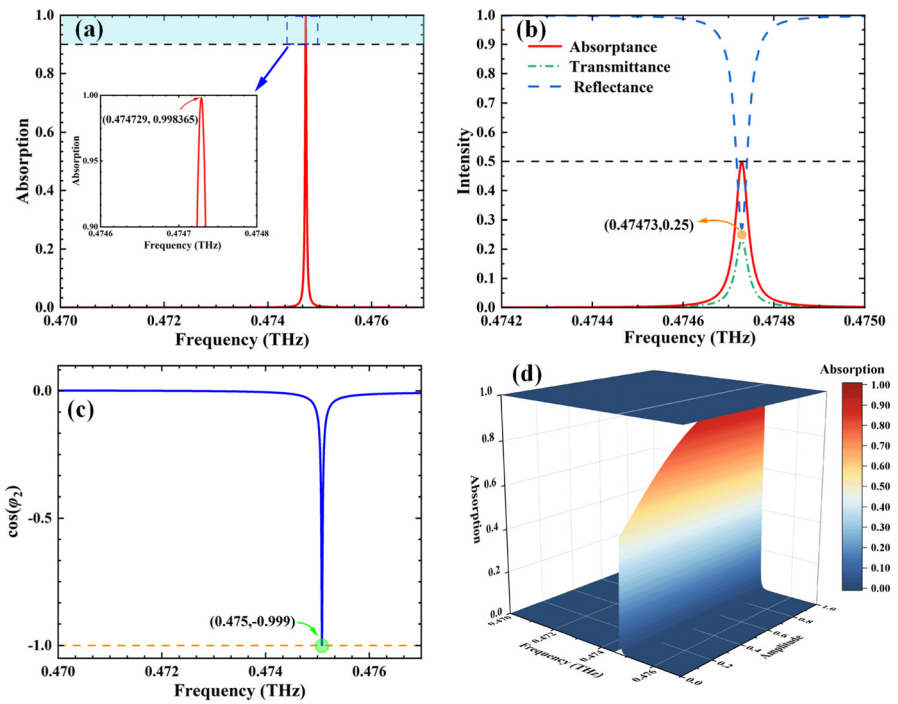

Fig. 2 (a) The absorption curve of the device when CPA is obtained. (b) The reflection and transmission curves in the situation of one-side incidence. (c) The CPA conditions are satisfied only when $\cos\Delta\varphi_2$ is equal to −1 or 1. (d) The 3-D plot demonstrates the link between the amplitude of incident waves and the absorption.

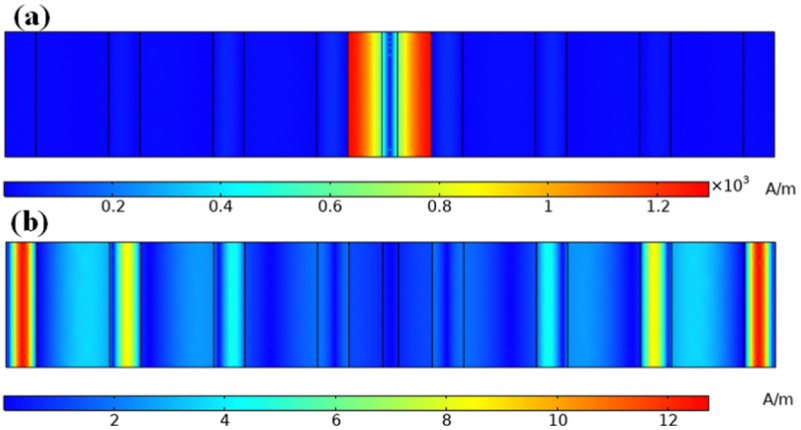

Fig. 3 The distribution of magnetic field at different frequencies simulated by the finite element method. (a) f = 0.46243 THz. (b) f = 0.47 THz.

As demonstrated in Fig. 4(a), when a layer of α-lactose loaded on the left side of Teflon film varied from 0.05 μm to 0.5 μm, the position of absorption peaks are 0.474943 THz, 0.474802 THz, 0.474521 THz, and 0.47368 THz and the intensities are 0.977, 0.933, 0.837, 0.633, respectively. One can find that their resonant frequencies remain almost constant while absorptions decrease significantly, which is because of the strong dependency on the material loss within the cavity at resonance and limited impact on the total optical path of thin layers of α-lactose. Fig. 4(b) displays the total transmittance at resonance as a function of the thickness of α-lactose, which exhibits a negative correlation linear property.

Based on the analysis above, it is evident that a slight change in the thickness of α-lactose to a large reduction in absorption, and the prospect of employing the amplitude of EM waves to increase absorption to realize optical THz fingerprint sensing will be studied next. According to theoretical research, the highest fluctuation in absorptance occurs around the absorptance of 0.5. Therefore, to realize amplitude modulation for sensing, the absorption is kept at 0.5 by adjusting the relative amplitude of EM waves. Because of the difficulty to measure the thickness of the α-lactose layer directly, by modulating the amplitude, sensors typically employ a specialized technique to connect the thickness to a measurable physical quantity and establish a bijective function to characterize this connection. As seen in Fig. 5(a), when the thickness of α-lactose differs from 0 μm to 0.5 μm, at 0.05 μm intervals, the amplitude-$d_{\alpha\text{-lactose}}$ is A = 0.78255 $d_{\alpha\text{-lactose}}$ − 0.02136, where A represents relative amplitude with the calculated R-square being 0.99386. The high R-square value demonstrates that its linearity remains excellent, which is propitious to designing an optical sensor.

When assessing an optical sensor, it is critical to consider S, Q FOM*, and DL. A sensor with excellent performance necessarily has a higher Q, higher S, higher FOM*, and lower DL. The following are the definitions., which are modulated to control absorption. ΔA, $\Delta d_{\alpha\text{-lactose}}$, denote relative amplitude and the thickness of α-lactose change, respectively. The resonance frequency is denoted by f_T, while the half-height breadth of the absorption peak is denoted by FWHM.[31,32]

$$A = \frac{|I_-|}{|I_+|}, \tag{22}$$

$$S = \frac{\Delta A}{\Delta d_{\alpha\text{-lactose}}}, \tag{23}$$

$$Q = \frac{f_T}{\mathrm{FWHM}}, \tag{24}$$

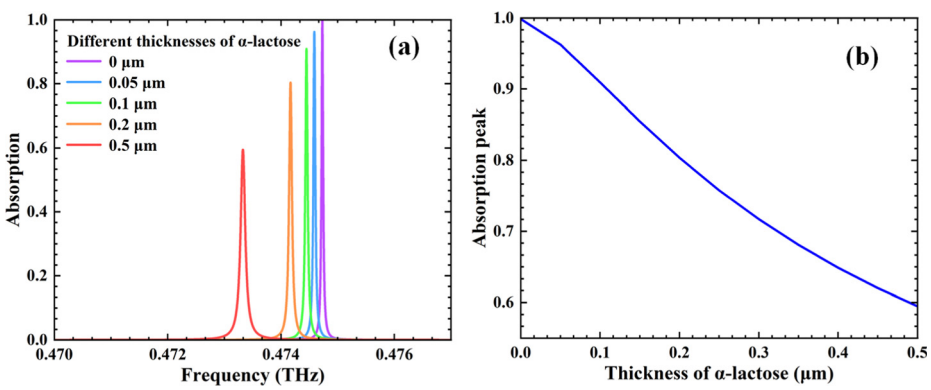

Fig. 4 (a) Absorption of the structure of the sensor with different thicknesses of α-lactose loaded on the left side of the Teflon film implanted in this cavity (b) dependence of α-lactose thickness on the maximum value of absorptance through this cavity at resonance.

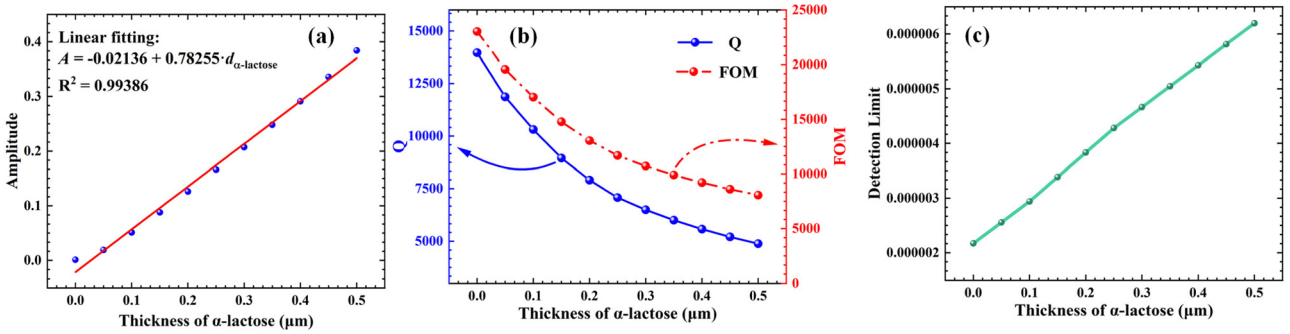

Fig. 5 (a) The linear relationship between the amplitude of incident waves corresponds to the thickness of the α-lactose layer at equal intervals. (b) Q and FOM* values at different thicknesses of the α-lactose layer. (c) The DL value at different thicknesses of the α-lactose layer.

The general FOM* created by J. Becker can be used to assess the performance of the whole sensor.[33] Its definition is that it is the biggest difference in relative intensity dI/I caused by a small variation in $d_{\alpha\text{-lactose}}$.

$$\mathrm{FOM}^{*} = \left(\frac{(\mathrm{d}I/I)}{d_{d_{\alpha\text{-lactose}}}}\right)_{\max}, \tag{25}$$

The DL is often used to denote the tiniest change that the optical sensor could detect:

$$\mathrm{DL} = \frac{f_{\mathrm{T}}}{20 \cdot S \cdot Q}, \tag{26}$$

According to the linear fitting curve shown in Fig. 5(a), the S can be obtained as 0.78255 μm^{-1}. Fig. 5(b) points out that the sensor maintains superior performance when detecting THz fingerprints, the highest Q value can reach 13 962.62, and the average Q value can be as high as 8019.2, which shows the high resolution of the sensor. Moreover, through calculation, the highest FOM* value is 23 016.18 (THz μm)$^{-1}$, and the average FOM* value attains 13 234.39 (THz μm)$^{-1}$. Similarly, the overall Q and FOM* values decrease as the thickness of the measured α-lactose layer increases. As depicted in Fig. 5(c), the detection limit of the optical sensor maintains a remarkably high level, with a calculated DL value of 2.1×10^{-6} at minimum. The excellent Q, FOM*, and DL values indicate the THz fingerprint sensor is sensitive to the thickness of α-lactose, and the detection accuracy is outstanding. The reproducible way to simulate their proposed structure can be found in Section S2 of ESI.†

2.3. The introduction of disorder effect

Given the great sensitivity of the detection of this device, it is necessary to investigate how the disorder effect in the dielectric layers alters the performance of the proposed sensing scheme. Fig. 6(a) demonstrates the Probability density function curves and random number values distribution concerning the normal distribution of physical quantities. If the actual physical parameters x of the dielectric layer obey a normal distribution with mean value μ and standard deviation σ, the probability density function is:

$$p(x) = \frac{1}{\sqrt{2\pi}\sigma} \mathrm{e}^{-\frac{(x-\mu)^2}{2\sigma^2}} \tag{27}$$

Herein, while the disorder effect is introduced in one of the dielectric layers, other parameters remain unchanged. In the three disorder situations, the random process is sampled for several times M = 100. The relative physical quantities of the dielectric layers distribution in the z-direction at different disorder intensities are indicated in Fig. 6(b)–(d).

As exhibited in Fig. 6, employing the TMM, the absorption spectra at normal incidence can be analyzed with four types of disorder. The first type is shown in Fig. 6(a), other parameters are maintained constant while introducing disorder to the thicknesses of air layers in a finite structure. The disorder introduced in air layers is with random thicknesses. A distribution exhibiting a normal distribution centered on a mean value of $\bar{d}_{\mathrm{air}}$ and a standard deviation of σ. When the standard deviation is as high as 10 μm, the ensemble-averaged absorption barely fluctuates. Therefore, the whole device is insensitive to manufacturing errors in the thickness of air layers. For the second type exhibited in Fig. 6(b), the disorder in the thicknesses of silicon layers is introduced in the same way as the random thicknesses d_{Si} follow a normal distribution around a mean value $\bar{d}_{\mathrm{Si}}$ with a standard deviation σ. The ensemble-averaged absorption scarcely alters when the standard deviation is up to 1 μm. Consequently, manufacturing errors in the thicknesses of silicon layers have a

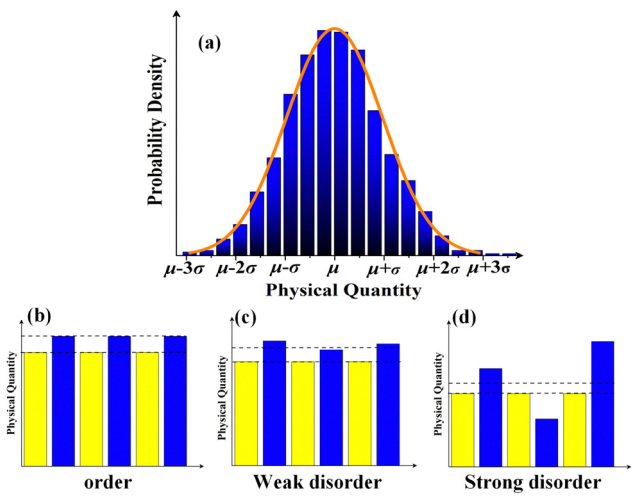

Fig. 6 (a) Probability density function curves and random number values distribution concerning the normal distribution of physical quantities. The ensemble-averaged absorptions under different disorder strength σ are displayed, (b) order, (c) weak disorder, (d) strong disorder.

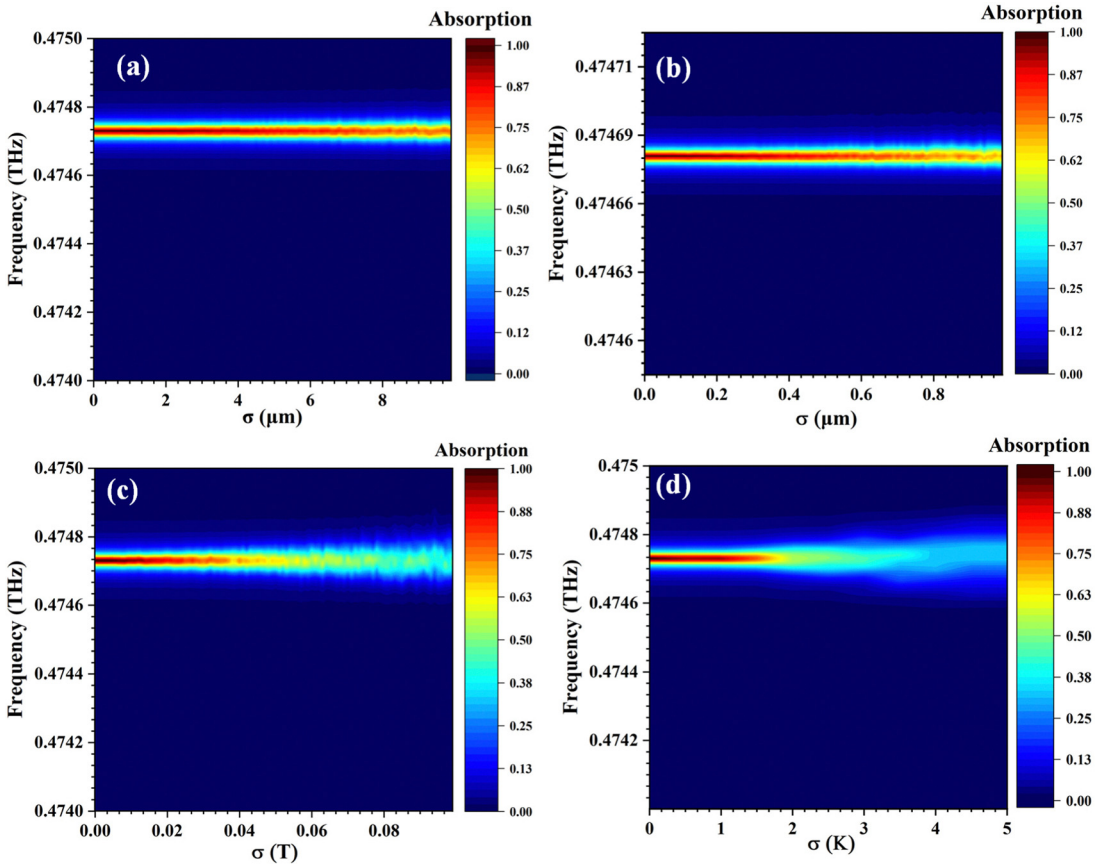

Fig. 7 Evolutions of the ensemble-averaged absorption for different types of disorder effect (a) disorder in the thicknesses of air layers. (b) disorder in the thicknesses of silicon layers. (c) disorder in the external magnetic field. (d) disorder in the temperature.

Table 1 The comparative evaluation of different works

Research	Measuring range	Amplitude sensing or not	S	Q	FOM	DL	Physical mechanism
Ref. 34	10–40 μm	No	5 GHz μm^{-1}	40	133 mm^{-1}	0.69	Not CPA
Ref. 35	—	No	—	1839	6.5	0.00096	Not CPA
Ref. 36	3.6–12.6 μm	No	0.001844 THz μm^{-1}	140 069	13 322 μm^{-1}	0.01250	Not CPA
This work	0–0.5 μm	Yes	0.78255 μm^{-1}	13 234.4	8019.2	4.21×10^{-6}	CPA

negligible effect on the entire device. For the following sorts, disorders in the external magnetic field and temperature are introduced in the same way shown in Fig. 6(c) and (d). The ensemble-averaged absorption rarely decreases, despite the standard deviations of the external magnetic field and temperature exceeding 0.04 T and 2 K, respectively. As a result, the overall device is little affected by changes in the sensing environment. The introduction of the disorder shows the optical sensor is insensitive to genuine manufacturing and environmental errors in the equipment, which demonstrates the excellent performance of the THz fingerprint sensor (Fig. 7).

To emphasize the distinctions between this optical sensor and conventional sensors, the performance metrics are presented in Table 1 for comparison. It can be found that the optical sensor has great advantages in its sensitivity and accuracy when the operating frequency is similar. In addition, we provide a feasible fabrication process and method for this sensing device, which can be found in Section S3 of ESI.†

3. Conclusion

In this paper, an optical THz fingerprint sensor is proposed and employs amplitude modulation for sensing. After the device successfully obtains CPA, the optical amplitude is adjusted to modify the absorptance to 0.5. The narrow absorption peak is extremely susceptible to changes in the thickness of the α-lactose layer due to the instability of CPA. Hence, when employed as the α-lactose of 0–0.5 μm measurement, the corresponding S is 0.78255 μm^{-1}, the average Q value is up to 8019.2, the average FOM* value is 13 234.4 $(THz\ \mu m)^{-1}$, and the lower DL is 4.21×10^{-6}. The influences of the disorder effect in

the dielectric layers are discussed extensively and the great practical application potential of the optical sensor is demonstrated by remarkable performance metrics.

Conflicts of interest

There are no conflicts to declare.

Notes and references

1 Y. D. Chong, L. Ge, H. Cao and A. D. Stone, Coherent perfect absorbers: time-reversed lasers, *Phys. Rev. Lett.*, 2010, **105**(5), 053901.

2 W. Wan, Y. Chong, L. Ge, H. Noh, A. D. Stone and H. Cao, Time-reversed lasing and interferometric control of absorption, *Science*, 2011, **331**, 889.

3 Y. D. Chong and A. D. Stone, Hidden black: Coherent enhancement of absorption in strongly scattering media, *Phys. Rev. Lett.*, 2011, **107**, 163901.

4 R. Ebrahimi Meymand, A. Soleymani and N. Granpayeh, All-optical AND, OR, and XOR logic gates based on coherent perfect absorption in graphene-based metasurface at terahertz region, *Opt. Commun.*, 2020, **458**, 124772.

5 M. Papaioannou, E. Plum, J. Valente, E. T. Rogers and N. I. Zheludev, Two-dimensional control of light with light on metasurfaces, *Light: Sci. Appl.*, 2016, **5**(4), e16070.

6 W. Wan, Y. Chong, L. Ge, H. Noh, A. D. Stone and H. Cao, Time-reversed lasing and interferometric control of absorption, *Science*, 2011, **331**(6019), 889–892.

7 A. Krasnok, D. Baranov, H. Li, M.-A. Miri, F. Monticone and A. Alú, Anomalies in light scattering, *Adv. Opt. Photonics*, 2019, **11**(4), 892–951.

8 E. Rezagholizadeh, M. Biabanifard and S. Borzooei, Analytical design of tunable THz refractive index sensor for TE and TM modes using graphene disks, *J. Phys. D: Appl. Phys.*, 2020, **53**(29), 295107.

9 M. Biabanifard, A. Arsanjani, M. S. Abrishamian and D. Abbott, Tunable terahertz graphene-based absorber design method based on a circuit model approach, *IEEE Access*, 2020, **8**, 70343–70354.

10 M. S. Islam, J. Sultana, M. Biabanifard, Z. Vafapour, M. J. Nine, A. Dinovitser and D. Abbott, Tunable localized surface plasmon graphene metasurface for multiband superabsorption and terahertz sensing, *Carbon*, 2020, **158**, 559–567.

11 A. Arsanjani, M. Biabanifard and M. S. Abrishamian, A novel analytical method for designing a multi-band, polarization-insensitive and wide angle graphene-based THz absorber, *Superlattices Microstruct.*, 2019, **128**, 157–169.

12 X. Shi and Z. H. Han, Enhanced terahertz fingerprint detection with ultrahigh sensitivity using the cavity defect modes, *Sci. Rep.*, 2017, **7**(1), 1–8.

13 S. Dey, S. Singh and D. N. Rao, High precision position sensor based on CPA in a composite multi-layered system, *Opt. Express*, 2018, **26**(8), 10079–10090.

14 C. Li, J. Qiu, J.-Y. Ou, Q. H. Liu and J. Zhu, High-Sensitivity Refractive Index Sensors Using Coherent Perfect Absorption on Graphene in the Vis-NIR Region, *ACS Appl. Nano Mater.*, 2019, **2**(5), 3231–3237.

15 Y. Zhang, F. P. Wu and H. F. Zhang, Theoretical Model of a RI THz Sensor Realized by Coherent Perfect Absorption With Optical Phase Modulation, *IEEE Sens. J. 22.15*, 2022, 14842–14850.

16 B. Han, Z. Han, J. Qin, Y. Wang and Z. Zhao, A sensitive and selective terahertz sensor for the fingerprint detection of lactose, *Talanta*, 2019, **192**, 1–5.

17 J. Zhu, S. Jiang, Y. Xie, F. Li, L. Du, K. Meng and J. Zhou, Enhancing terahertz molecular fingerprint detection by a dielectric metagrating, *Opt. Lett.*, 2020, **45**(8), 2335–2338.

18 S. Ding, J. Y. Ou, L. Du, L. Zhu, S. A. Khan, H. Chen and J. Zhu, Enhancing ultra-wideband THz fingerprint sensing of unpatterned 2D carbon-based nanomaterials, *Carbon*, 2021, **179**, 666–676.

19 R. Kitamura, L. Pilon and M. Jonasz, Optical constants of silica glass from extreme ultraviolet to far infrared at near room temperature, *Appl. Opt.*, 2007, **46**(33), 8118–8133.

20 S. Chen, F. Fan, X. Wang, P. Wu, H. Zhang and S. Chang, Terahertz isolator based on nonreciprocal magneto-metasurface, *Opt. Express*, 2015, **23**(2), 1015–1024.

21 J. Sui, D. Zhang and H. Zhang, Logical OR operation and magnetic field sensing based on layered topology, *J. Phys. D: Appl. Phys.*, 2022, **55**(41), 415001.

22 S. S. Rao, J. T. Zhang and H. F. Zhang, A multifunctional and multiscale device of magnetic-controlled AND logical operation and detection based on the nonreciprocity of the magnetized InSb photonic structure, *Results Phys.*, 2021, **31**, 105058.

23 J. Y. Sui, Y. M. Liu and H. F. Zhang, A device of XOR logic gate and multiscale sensing based on layered topology, *Waves Random Complex Media*, 2023, 1–22.

24 L. Qi, Z. Yang, F. Lan, X. Gao and Z. Shi, Properties of obliquely incident electromagnetic wave in one-dimensional magnetized plasma photonic crystals, *Phys. Plasmas*, 2010, **17**(4), 042501.

25 G. P. Knifn and L. M. Zurk, Model-based material parameter estimation for terahertz refection spectroscopy, *IEEE Trans. Terahertz Sci. Technol.*, 2012, **2**, 231–241.

26 Z. Han, A. M. Soehartono, B. Gu, X. Wei, K. T. Yong and Y. Shi, Tunable hybridization induced transparency for efficient terahertz sensing, *Opt. Express*, 2019, **27**(6), 9032–9039.

27 A. Roggenbuck, H. Schmitz, A. Deninger, I. C. Cámara Mayorga, J. Hemberger, R. Güsten and M. Grüninger, Coherent broadband continuous-wave terahertz spectroscopy on solid-state samples, *New J. Phys.*, 2010, **12**(4), 043017.

28 J. Sui, R. Dong, S. Liao, Z. Zhao, Y. Wang and H. F. Zhang, Janus Metastructure Based on Magnetized Plasma Material with and Logic Gate and Multiple Physical Quantity Detection, *Ann. Phys.*, 2023, 2200509.

29 R. Ning, S. Liu, H. Zhang, B. Bian and X. Kong, A wide-angle broadband absorber in graphene-based hyperbolic 16 metamaterials, *Eur. Phys. J.: Appl. Phys.*, 2014, **68**(2), 20401.

30 W. Zhu, F. Xiao, M. Kang and M. Premaratne, Coherent perfect absorption in an all-dielectric metasurface, *Appl. Phys. Lett.*, 2016, **108**(12), 121901.
31 Z. A. Zaky, A. M. Ahmed, A. S. Shalaby and A. H. Aly, Refractive index gas sensor based on the Tamm state in a one-dimensional photonic crystal: Theoretical optimisation, *Sci. Rep.*, 2020, **10**(1), 973.
32 B.-F. Wan, Q.-Y. Wang, H.-M. Peng, H.-N. Ye and H.-F. Zhang, A Late-Model Optical Biochemical Sensor Based on OTS for Methane Gas and Glucose Solution Concentration Detection, *IEEE Sens. J.*, 2021, **21**(19), 21465–21472.
33 J. Becker, A. Trügler, A. Jakab, U. Hohenester and C. Sönnichsen, The Optimal Aspect Ratio of Gold Nanorods for Plasmonic Bio-sensing, *Plasmonics*, 2010, **5**, 161–167.
34 Z. Y. Zhang, F. Fan, T. F. Li, Y. Y. Ji and S. J. Chang, Terahertz polarization conversion and sensing with double-layer chiral metasurface, *Chin. Phys. B*, 2020, **29**(7), 078707.
35 S. Sun, Q. Song and S. Xiao, Rapid and nondestructive determination of graphene thickness with an all dielectric metasurface, *Plasmonics*, 2017, **12**(6), 1685–1691.
36 J. T. Zhang, S. S. Rao and H. F. Zhang, Dual-mode High-Q Multiphysics Sensor Based on the Evanescent Wave in the InSb Photonic Crystals, *IEEE Sens. J.*, 2022, 10500–10507.